Environmental Science and Pollution Research (2019) 26:5020–5037
https://doi.org/10.1007/s11356-018-4035-2

RESEARCH ARTICLE

Highly adsorptive chitosan/saponin-bentonite composite film for removal of methyl orange and Cr(VI)

Livy Laysandra[1] · Immanuel Joseph Ondang[1] · Yi-Hsu Ju[2] · Benedikta Hervina Ariandini[1] · Agatha Mariska[1] · Felycia Edi Soetaredjo[1] · Jindrayani Nyoo Putro[3] · Shella Permatasari Santoso[1] · Farida Lanawati Darsono[4] · Suryadi Ismadji[1]

Received: 25 September 2018 / Accepted: 17 December 2018 / Published online: 2 January 2019

Abstract

Robust and simple composite films for the removal of methyl orange (MO) and Cr(VI) have been prepared by combining chitosan, saponin, and bentonite at a specific ratio. There are several composite films (chitosan-saponin-bentonite (CSB)) prepared; among them, the composite films $CSB_{2:3}$ and $CSB_{1:1}$ have the highest removal efficiency toward MO and Cr(VI) where the maximum removal is 70.4% (pH 4.80) and 92.3% (pH 5.30), respectively. It was found that different types of adsorbate have different thermodynamic properties of the adsorption process; the adsorption of MO onto $CSB_{2:3}$, chitosan, and acid-activated bentonite (AAB) proceeded endothermically, while the adsorption of Cr(VI) onto $CSB_{1:1}$, chitosan, and AAB proceeded exothermically. The parameters of the adsorption were modeled by using isotherm and kinetic equations. The models of Langmuir, Freundlich, Redlich-Peterson, Sips, and Toth were used for fitting the adsorption isotherm data at a temperature of 30, 45, and 60 °C; all of the isotherm models could represent the data well. The result indicates that $CSB_{2:3}$ has the highest adsorption capacity toward MO with q_m of 360.90 mg g^{-1} at 60 °C; meanwhile, $CSB_{1:1}$ has the highest adsorption capacity toward Cr(VI) with q_m 641.99 mg g^{-1} at 30 °C. The pseudo-second-order model could represent the adsorption kinetics data better than the pseudo-first-order equation. The adsorption mechanism was proposed, and the thermodynamic properties of the adsorption were also studied.

Keywords Ca-bentonite · Saponin · Chitosan · Anionic dyes · Heavy metals: CSB film

Responsible editor: Tito Roberto Cadaval Jr

Electronic supplementary material The online version of this article (https://doi.org/10.1007/s11356-018-4035-2) contains supplementary material, which is available to authorized users.

✉ Felycia Edi Soetaredjo
felyciae@yahoo.com

✉ Suryadi Ismadji
suryadiismadji@yahoo.com

[1] Department of Chemical Engineering, Widya Mandala Surabaya Catholic University, Kalijudan 37, Surabaya 60114, Indonesia

[2] Graduate Institute of Applied Science, National Taiwan University of Science and Technology, 43 Keelung Road, Sec 4, Taipei 10607, Taiwan

[3] Department of Chemical Engineering, National Taiwan University of Science and Technology, 43 Keelung Road, Sec 4, Taipei 10607, Taiwan

[4] Faculty of Pharmacy, Widya Mandala Surabaya Catholic University, Pakuwon City, Kalisari 1, Surabaya 60112, Indonesia

Introduction

Synthetic dyes are widely used to color many industrial products such as textile, paper, plastics, and leather (Chiou and Li 2002). In most cases, untreated synthetic dye wastes can cause pollution of the aquatic environment and also poison its biota. The improper treatment of water containing dyes may even lead to significant damage to the daily used water; it may cause pollution and produce unpleasant odor and color to the water bodies. Dye-contaminated water is also known to have an increased level of biochemical oxygen demand (BOD), chemical oxygen demand (COD), and total suspended solids. Heavy metals are also known to cause severe water pollution. Heavy metal pollution has been considered to be more toxic to public health than that of synthetic dyes. The toxicity of the heavy metals is due to its mutagenic, carcinogenic, and non-biodegradable properties (Hu et al. 2011).

There are some methods those are frequently used for the treatment of wastewater, specifically adsorption, electrocatalytic

degradation, and membrane filtration (Walker et al. 2003). As shown in Table 1, adsorption is the preferable method for the removal of dyes and heavy metal such as chromium. Adsorption is a favorite method because of its simplicity in design and operation, high efficiency, high availability, and easy scaling up (Hamdaoui 2006); other methods have high operational costs, difficult to regenerate, and sometimes cause secondary pollution. While adsorption is an excellent wastewater treatment process, the effectiveness of the process entirely depends on the choice of the adsorbent and operating conditions. Many types of researches are dedicated to the development of cheap, robust, and low-cost adsorbents which are high in adsorption capacity and easy to prepare. A lot of composite or hybrid materials (Table 1) were designed prior to develop a potential adsorbent (removal material); some of them are hydroxyapatite/chitosan composite, cellulose-montmorillonite composite, core@double-shell nano-hybrids, and clay-filled hydrogels.

Chitosan (beta-1,4-polyglucosamine) is a natural compound derived from *N*-deacetylation of chitin using alkaline compounds. Chitin can be obtained from the extraction of crustacean exoskeleton, insect cuticle, and fungal cell wall (Crini and Badot 2008; Dotto et al. 2013). Chitosan has been proven to be a potential adsorbent. The adsorption ability of chitosan is supported by its amine ($–NH_2$) and hydroxyl (–OH) groups; these groups possess high electrostatic attraction that could help to bind the adsorbate molecules. There are several chitosan-based adsorbents that have been developed. However, to the best of our knowledge, they still have relatively low adsorption capacity (Hena 2010; Huang et al. 2017; Jung et al. 2013; Leodopoulos et al. 2012; Li et al. 2015; Udaybhaskar et al. 1990; Wu et al. 2012; Zeng et al. 2015; Zhu et al. 2010). Therefore in this work, the chitosan adsorption capacity is further increased by incorporating with bentonite and saponin. Bentonite and saponin were chosen since they are natural, cheap, and abundantly reserve. Bentonite has been ubiquitously accepted as the superior material for wastewater treatment. Bentonite is hydrated aluminasilicate clay; it is mainly composed by the smectite montmorillonite group minerals (Tahir and Rauf 2006). Bentonite has a permanent negative surface charge at its three-layered structure of silicate-alumina which is usually offset by exchangeable cations of Na^+ and Ca^{2+}; this negative surface charge helps to attract the oppositely charge adsorbate molecules (Laysandra et al. 2017). Bentonite also possesses a high specific surface area that made it a highly potential adsorbent. Another material used is rarasaponin (saponin), natural surface-active molecules extracted from the fruit or root of *Sapindus rarak* DC (soapberry). The bentonite and chitosan were chosen for the preparation of chitosan-saponin-bentonite (CSB) composite film due to their potential adsorption ability. Saponin is a surface modifying agent, and the addition of saponin leads to surface alteration through chemical interaction of its two acyl groups (Kurniawan et al. 2011).

The CSB was incorporated into a composite film through a simple preparation method. The prepared CSB composite films show a superior adsorption process with a very high adsorption capacity compared to the similar adsorbent materials. Furthermore, in this work, we have demonstrated practical and straightforward incorporation of chitosan-saponin-bentonite into composite films. Different saponin-bentonite and chitosan ratios were combined to prepare different CSB. Adsorption experiments in batch mode against methyl orange (MO) and Cr(VI) were conducted to examine the adsorption capacity of this new adsorbent, the CSB composite. The kinetic, isotherm, and thermodynamic models and equations

Table 1 Some techniques for removal of hazardous compounds from water

Hazardous compounds	Removal technique	Removal material	Reference
Congo red	Adsorption	Hydroxyapatite/chitosan composite	Hou et al. 2012
Congo red	Adsorption	Clay-filled hydrogels of polyacrylic acid and polyethylene glycol	Bhattacharyya and Ray 2015
Acid brown 14	Electrocatalytic degradation	–	Bassyouni et al. 2017
Methylene blue	Adsorption	Core@double-shell structured magnetic halloysite nanohybrids	Wan et al. 2017
Methylene blue	Adsorption	Cellulose-montmorillonite composite	Santoso et al. 2017
Organic micropollutants (pharmaceuticals, personal care products, and pesticides)	Submerged membrane filtration	Granular activated carbon	Shanmuganathan et al. 2016
Direct Blue 14	Membrane filtration	Nanofibrous composite membrane from poly(arylene ether nitrile)/bioinspired polydopamine-coated graphene oxide	Zhan et al. 2017
Cr(VI)	Adsorption	Bamboo-like polypyrrole nanofibrous mats	Zhan et al. 2018
Methylene blue, rhodamine-WT, triclosan, and triclocarban	Membrane filtration	Graphene oxide membranes	Oh et al. 2017

were used to characterize the adsorption of MO and Cr(VI) onto CSB.

Materials and methods

Material and the preparation of the composite films

All chemicals used in this study ($K_2Cr_2O_7$, 1,5-diphenylcarbazide, H_3PO_4, H_2SO_4, and CH_3COOH) were purchased from Sigma-Aldrich as an analytical grade and directly used without any further treatment. Analytical grade MO C.I. 13025 ($C_{14}H_{14}N_3NaO_3S$, MW 327.34 g/mol) and chitosan were also purchased from Sigma-Aldrich.

The raw bentonite used in this study was obtained from Pacitan, East Java, Indonesia. The bentonite was activated using 3 N of the H_2SO_4 solution, with the ratio of 1:3 *b*/*v*. The acid activation process was done at 100 °C for 2 h, under constant stirring 500 rpm. The resulting bentonite suspension was sonicated for 2 h at 35 °C. The obtained acid-activated bentonite (AAB) was then centrifuged and washed by using warm deionized water (80 °C) until the pH of the rinse water equal to the pH of deionized water. The AAB was dried using force circulated oven at 105 °C and irradiated using the microwave (National NN-S327 WF) at 700 W. Subsequently, the particle size was reduced into powder using micro-hammer mill (Janke and Kunkel) and sieved to get powder with the particle size − 180/+ 200 mesh using vibration screen (Retsch AS-200).

Soapberry fruits (*Sapindus rarak* DC) were purchased from Klaten, Central Java, Indonesia. The soapberry fruits were washed and sun-dried for 3 days. The dried soapberry fruits were then grounded and sieved to a particle size of − 180/+ 200 mesh. The saponin was extracted from the soapberry powder by adding deionized water with a ratio of 1:15 *w*/*v*; the mixture was then stirred and heated at 100 °C for 1 h. The supernatant was then separated from the solid by centrifugation (Hettich Zentrifugen EBA-20) at 4900 rpm for 4 min and concentrated by vacuum evaporation (BUCHI RE 121) at 80 °C for 3 h. The concentrated supernatant was then dried by using an oven (Memmert UM 400) at 60 °C overnight and then pulverized by using a micro-hammer mill and stored in a desiccator.

The CSB composite film was prepared by dissolving 1 g of saponin in 100 ml distilled water. Subsequently, 10 g of bentonite was added and stirred at 300 rpm for 30 min at 80 °C. The saponin-bentonite solid was separated by using centrifugation and dried at 105 °C overnight. Dried saponin-bentonite was pulverized and then sieved to − 180/+ 200 mesh particle size. A certain mass of saponin-bentonite was added to the 1 g of chitosan in 1 M of CH_3COOH solution. Different mass ratios of saponin-bentonite and chitosan of 1:1, 1:2, 2:1, 2:3, and 3:2 were used to prepare different CSB films, specifically $CSB_{1:1}$, $CSB_{1:2}$, $CSB_{2:1}$, $CSB_{2:3}$, and $CSB_{3:2}$, respectively. The mixture was stirred at 500 rpm for 2.5 h, at 80 °C. The resulting mixture was then dried in the oven at 60 °C and kept in the desiccator until subsequent use.

Characterization of adsorbents

Fourier transform infrared spectroscopy (FTIR) spectra were collected by using a Shimadzu 8400S spectrometer (SpectraLab Scientific, ON) with an accumulation of 128 scans in the wavenumber range from 4000 to 400 cm^{-1}. Nitrogen sorptions at 77 K were conducted on a Micromeritics ASAP 2010 analyzer (Micromeritics Instrument Corp., GA). Scanning electron microscopy (SEM) images were collected by using a JEOL JSM-6500F SEM (JEOL, Japan) at an accelerating voltage of 10.0 kV. The X-ray diffraction (XRD) analyses were performed by using a Philips X'Pert X-Ray diffractometer (Rigaku Corp., Tokyo) with CuKα radiation ($\lambda = 0.15406$ nm), operated at 30.0 kV and 10.0 mA.

Adsorption experiments

In all of the adsorption experiments, MO and $K_2Cr_2O_7$ were used as the adsorbate. To assess the effect of pH on the adsorption capacity, batch adsorption studies were performed at various pH levels (2.00–8.00) of the solution. The pH of the solution was adjusted by using 0.1 M NaOH or 0.1 M HCl solution. The adsorption was conducted at 30 °C for 3 h. After 3 h, the concentration of the adsorbate was determined by using the spectrophotometric method.

For the determination of the point of zero charges (pH_{pzc}), a pH drift method was used. Briefly, a series of 50 ml 0.01 M NaCl solutions were prepared in capped Erlenmeyer flasks. The pH of each solution was adjusted to different values between 2 and 8 by dropwise addition of 0.1 M NaOH or 0.1 M HCl solution. Subsequently, 0.2 g of adsorbent was added to each flask and shaken for two consecutive days. The initial and final (after shaken) pH values were determined by using a pH meter (Schoot CG-825). The pH_{pzc} is defined as the cross point between final pH and initial pH.

The adsorption isotherm studies were carried out by mixing various mass of adsorbents into a series of iodine flasks containing 100 ml solution of MO and Cr(VI). The adsorption isotherm studies were conducted at 30, 45, and 60 °C in a thermostated water bath (Memmert SV-1422), with a constant shaking speed of 200 rpm. The adsorption was performed until the equilibrium condition was achieved, which is 150 min in this study (as found from preliminary kinetic adsorption study, the concentration of the adsorbate still slightly increased at 120–130 min and remained constant (equilibrium) afterwards). The

adsorption removal efficiency (η, %) and amount of solute adsorbed (q_e, mg g^{-1}) were calculated by Eqs. (1) and (2).

$$\eta = \frac{C_0 - C_i}{C_0} \times 100\% \quad (1)$$

$$q_e = \frac{(C_0 - C_i)}{m} \times V \quad (2)$$

where C_0 and C_i represent the initial and equilibrium concentrations of solute (mg l^{-1}), respectively; m and V represent the mass of adsorbent (g) and the volume of solution (l), respectively.

The kinetics adsorption studies were conducted at several initial adsorbate concentrations of 100, 200, 300, 500, and 700 ppm. 0.5 g of the adsorbent was added to each concentration. The adsorption was then performed in a thermostated water bath at 30 °C and constant shaking speed of 200 rpm. The sampling was taken at a 15-min interval. The amount of solute adsorbed by the solid at a particular time (q_t) was determined by using Eq. (3).

$$q_t = \frac{(C_0 - C_t)}{m} \times V \quad (3)$$

where C_t is the concentration of solute at certain time t.

The concentrations of the solutes were determined by using a spectrophotometer (Shimadzu UV/VIS-1700 PharmaSpec) at maximum wavelengths of 491 and 543 nm for MO and Cr(VI), respectively. A series of MO and Cr(VI) solution at different concentrations was prepared prior to prepare a standard curve. Particularly for Cr(VI) ions, the concentration was determined as follows: 1 ml of 0.02 M 1,5-diphenylcarbazide solution in acetone was added into 0.4 ml of a sample containing Cr(VI), then 0.25 N H_2SO_4 solution was added to a total volume of 10 ml. All experiments were conducted in triplicate, and the average results were presented.

Result and discussion

Characteristics of CSB

Table 2 provides the FTIR spectra of the surface functional groups of AAB, chitosan, $CSB_{1:1}$, and $CSB_{2:3}$ before and after adsorption. The FTIR spectra are presented as Supplementary Data in Figures S1 and S2. FTIR peaks at wavenumbers of 3843.9, 3639.4, 2970.2, 1668.3, and 929.6 cm^{-1} were observed for AAB; those peaks correspond to the stretching and bending vibrations of O–H groups. The peaks at 1039.6 cm^{-1} and 669.2 cm^{-1} are due to the silanol stretches from Si–O–Si on tetrahedral and Si–O sheets on silica and quartz, while the peak at 516.9 cm^{-1} is due to the Al–O–Si bend. For saponin, the peak at 1249.8 cm^{-1} is due to the stretching of C=O stretch. The main peaks for chitosan that occur at 3492.8 and 3448.5 cm^{-1} are due to vibration stretching of O–H and N–H, peak at 1622.0 cm^{-1} is due to stretching NH_2, peak at 1502.4 cm^{-1} is due to N–H bending, and peak at 1415.6 cm^{-1} is due to vibrations of O–H and C–H in the amide ring (Kurniawan et al. 2011; Paluszkiewicz et al. 2011).

The formation of CSB indicates by the occurrence of the peaks of silanol (Si–OH), deacylated C=O, amine (N–H), silanol groups, deacylated carbonyl groups, and amine groups as summarized in Table 1. The presence of the mentioned functional groups on the CSB indicates that all of the materials (chitosan, saponin, and bentonite) were successfully incorporated in the composite material.

The occurrence of new peaks and shifts of peaks due to the adsorption of MO and Cr(VI) on the composite film are observed in several surface functional groups. A new peak at 1369.4 cm^{-1} is observed for MO-loaded $CSB_{2:3}$; this new peak was associated with the SO_3^- group in the MO structure (Zhang et al. 2015). For the $CSB_{1:1}$, after the adsorption of Cr(VI), there are several shifts in peak that is observed; specifically, the peak for O–H stretch of phenols shifted from 3865.1 to 3849.6 cm^{-1}, peak for Si–OH shifted from 2908.4 to 2947.0 cm^{-1}, and peak for Al–Al–OH shifted from 935.4 to 950.8 cm^{-1}. The NH_2 shift in the chitosan amino group was also observed for $CSB_{1:1}$ loaded with Cr(VI) (from a wavenumber of 1652.9 to 1650.9 cm^{-1}). Based on these results of the functional group analysis above, the typical properties of CSB in the form of surface functional groups play an essential role in the adsorption of Cr(VI) or MO from aqueous solution. The amino (NH_2) and hydroxyl (OH) groups of chitosan are the principal receptors which are responsible for the binding of dyes and metal ions.

The SEM images of AAB, bentonite-saponin, $CSB_{1:1}$, and $CSB_{2:3}$ are shown in Fig. 1. The images were obtained at the same magnification of × 10,000. The results indicate that all of the materials possessed a rough surface topography which represents the presence of bentonite particles. The addition of saponin causes the decrease in coarseness of the smectite group crystal, thus resulting in a smoother surface of bentonite-saponin (Fig. 1b). The surface morphological change due to the incorporation of chitosan is significantly visible, where both of $CSB_{1:1}$ and $CSB_{2:3}$ have smoother surface morphologies than that of bentonite and bentonite-saponin. The smooth surface is due to the consolidation of the bentonite-saponin particles by chitosan forming a film. The formation of the film was indicated by the finely foliated surface of the $CSB_{1:1}$ and $CSB_{2:3}$. The addition of more chitosan resulted in more robust consolidation of the bentonite-saponin particle into a film, which can be indicated by the more even surface consistency in $CSB_{2:3}$ (Fig. 1d) than that of $CSB_{1:1}$ (Fig. 1c).

The XRD spectra of the adsorbents are given in Fig. 2. The broad hump at $2\theta = 15°–30°$ with the highest peak at 20° is referring to the diffraction characteristic of chitosan. In AAB,

Table 2 FTIR spectra of the functional group for the raw materials and CSB before and after adsorption

Functional group	AAB	Saponin	Chitosan	$CSB_{1:1}$		$CSB_{2:3}$	
				Pristine	Cr(VI)-loaded	Pristine	MO-loaded
O–H stretch (phenols)	3843.9	–	–	3865.1	3849.6	3865.1	3863.1
O–H stretch for H_2O in the silica matrix	3639.4	–	–	3625.9	3625.9	3635.6	3635.6
O–H stretch, free hydroxyl	–	3546.8	3492.8	3489.0	3489.0	3490.9	–
N–H stretch (1° or 2° amines)	3452.3	–	3448.5	3467.8	–	3467.8	–
O–H (Si–OH) groups	2970.2	–	–	2908.4	2947.0	–	–
C–H stretch	–	2933.5	3030.0	3062.7	3082.0	3016.5	3020.3
C=C stretch (alkynes)	2264.3	2356.8	2343.3	2341.4	2343.3	2347.2	2345.3
C=O in amide group	–	–	1780.2	1747.4	–	1747.4	–
C=O stretch (carbonyl group)	–	1724.2	–	1728.1	–	1728.1	–
O–H bend, for adsorbed H_2O at bentonite interlayer	1668.3	–	–	–	–	–	–
NH_2 in amino group	–	–	1622.0	1652.9	1650.9	1652.9	1622.0
NH bending vibration		–	1502.4	1519.8	1519.8	1519.8	1539.1
C–CH_3 bend	–	1448.4	–	1444.6	1461.9	–	–
O–H vibration in amide ring	–	–	1415.6	1425.3	–	1425.3	–
C–H bend bonded with hydroxyl group	–	1394.4	–	1392.5	1392.5	1392.5	–
$–SO_3^-$ groups	–	–	–	–	–	–	1369.4
C–H vibration in amide ring	–	–	1321.1	1321.1	–	1321.1	–
C=O stretch of deacylated carbonyl group	–	1249.8	–	1265.2	1265.2	1255.6	–
C=C stretch (ethers group)	–	1018.3	–	–	–	–	–
Si–O–Si stretch of the tetrahedral sheet	1039.6	–	–	1051.1	–	–	–
Al–Al–OH bend	929.6	–	–	935.4	950.8	941.2	958.6
Si–O stretching	669.2	–	–	671.2	671.2	671.2	680.8
Al–O–Si bend	516.9	–	–	522.7	530.4	–	547.7
Si–O–Si bend	455.2	–	–	453.2	–	453.2	466.7

the montmorillonite crystal plane indicates from the diffraction peaks at $2\theta = 20°$, 21.3°, and 35.9°; feldspar crystal plane indicates from the peak at $2\theta = 22.5°$; and quartz crystal plane indicates from the peak at $2\theta = 27.6°$. The combination of saponin, bentonite, and chitosan to form CSB caused a decrease in the crystallinity degree of the composites; this indicates by the weakening of the diffraction intensity especially at $2\theta = 20°$. The diffraction peaks of $CSB_{1:1}$ and $CSB_{2:3}$ are contributed from all of the precursor materials.

The internal texture of the adsorbents was examined by using nitrogen sorption method, and the results are depicted in Supplementary Data Figure S3. An H_2 type hysteresis loop is observed in AAB; this indicates that AAB has a complex network structure caused by interconnections between layers which create a bottleneck structure (Bahranowski et al. 2017). The broad hysteresis loop of AAB which starts at relative pressure (p/p^o) 0.5 signifies a type II isotherm and mesoporous structure; while at p/p^o below 0.5, the narrow loop signifies a type I isotherm and microporous structure. A combination between type II and type III isotherms is observed for $CSB_{1:1}$ and $CSB_{2:3}$, while chitosan has type III isotherm. Type III isotherm indicates a multilayered structure, thus confirming the formation of film layers. The pore size distribution (PSD) of the adsorbents are given as the inset in Supplementary Data Figure S3. The density functional theory (medium regularization) was employed to determine the PSD. A combination between micropore and mesopore structures are observed for AAB. The mesopore structure in conjunction with a small amount of micropore is observed for $CSB_{1:1}$ and $CSB_{2:3}$, while for chitosan, only mesopore structure is observed.

The determination of pH_{pzc} and the effect of pH

Change in pH affects the surface charge of the adsorbent. The positive or negative charge can be determined by comparing the pH of the solution against the point of zero charges (pH_{pzc}). As shown in Supplementary Data Figure S4, the pH_{pzc} for raw chitosan and AAB is 5.13 and pH 5.84, respectively; it indicates that both materials are acidic since the $pH_{pzc} < 7.00$; the surface charges are positive before pH of the solution reached pH_{pzc} and negative as pH of the solution exceed pH_{pzc}.

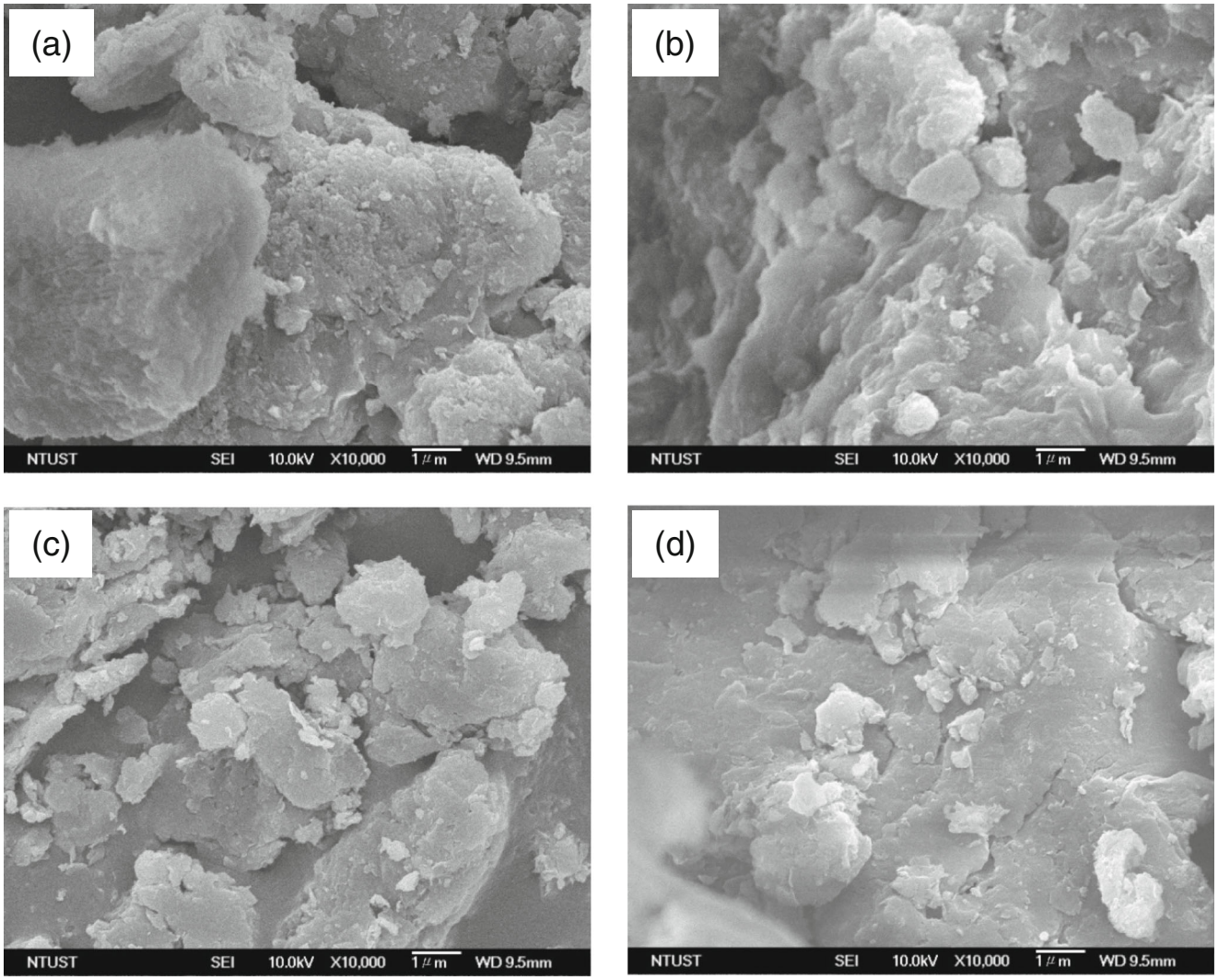

Fig. 1 SEM images of **a** acid-activated bentonite, **b** bentonite-saponin, **c** $CSB_{1:1}$ film, and **d** $CSB_{2:3}$ film

The effect of the initial pH of the solution on the adsorption of MO and Cr(VI) is shown in Fig. 3. The highest removal efficiency of MO by chitosan was 61.92% at pH 4.01; the removal efficiency decreases as the pH > 5.00. The highest removal efficiency of MO by AAB was 60.58%, and it was achieved at pH 5.07. For the adsorption of Cr(VI), the highest removal efficiency was achieved at pH 4.00 and 5.00 for AAB and chitosan, respectively. For the composite films ($CSB_{1:1}$, $CSB_{1:2}$, $CSB_{2:1}$, $CSB_{2:3}$, and $CSB_{3:2}$), the highest removal efficiency (70.4–92.3%) of MO and Cr(VI) was achieved at pH of 4.80–5.30. The $CSB_{2:3}$ and $CSB_{1:1}$ have the highest removal efficiency against MO and Cr(VI), respectively, compared to the others.

The formation mechanisms of CSB

To obtain a better understanding of the synthesis of CSB from bentonite, saponin, and chitosan, the following mechanisms are proposed. The bentonite and saponin were initially incorporated before adding the chitosan to form CSB. There are three main steps of saponin-bentonite incorporation as proposed by Kurniawan et al. 2011, briefly:

1. The deacylation of saponin by the polar solvent. The deacylation occurs on the two acyl ($–C_2H_3O^+$) groups which present in the carbonyl structure. The release of these two acyl groups leaves two negatively charged oxygen atoms on both carbonyl surfaces.
2. The silanol group (Si–OH) in bentonite attacked by the excess of H^+ ions in the solution to form $Si–OH_2^+$.
3. The imbalance charge on the surface of silanol is surmounted by the binding of negatively charged oxygen atoms from deacylated carbonyl groups.

The formation of CSB is initiated by the addition of acidic (acetic acid) chitosan solution into saponin-bentonite suspension. In solution, the $–NH_2$ group of chitosan is protonated to $–NH_3^+$. The acetate ion stabilizes the positive charge of –

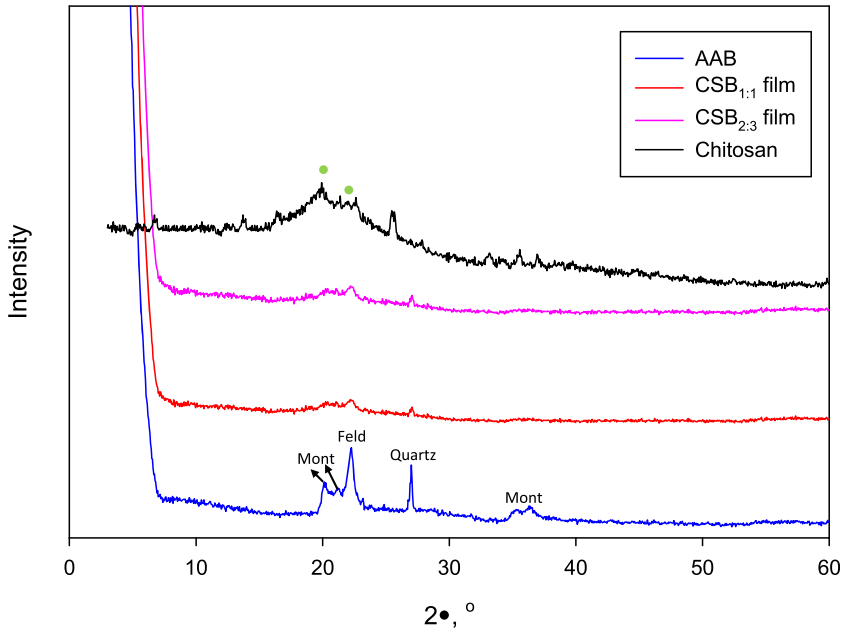

Fig. 2 XRD diffractograms of AAB, $CSB_{1:1}$, $CSB_{2:3}$, and chitosan. Symbols "Mont," "Feld," and "Quartz" stand for montmorillonite, feldspar, and quartz, respectively. The green circles denote the peaks that correspond to chitosan

NH_3^+ by forming the $–NH_3^+CH_3COO^-$. The presence of a large number of excess H^+ ions forms acetic acid that attacks the $–CH_2–OH$ group of chitosan to become $–CH_2–OH_2^+$. Meanwhile, the saponin-bentonite molecule is deacylated as it is suspended in polar solvent. Subsequently, the deacylated saponin group in saponin-bentonite molecule attached to the $–CH_2–OH_2^+$ of chitosan as it is added to the acidic chitosan solution. The schematic diagram of the formation mechanism is given in Fig. 4.

Adsorption mechanisms

As indicated from the pH study, the change of pH has affected the MO and Cr(VI) removal efficiency. The adsorption mechanism is proposed in Fig. 5. All of the adsorbents demonstrate a high removal efficiency as the pH of the solution approaching pH_{pzc}; this is due to the charge difference between the adsorbent and adsorbate. The adsorbent has a positive charge while the adsorbate has a negative charge. The negative charge of MO contributes from the sulfonate ($–SO_3^-$) group, while Cr(VI) occurs as $HCrO_4^-$ species at pH between 2.00 and 8.00 and as CrO_4^{2-} species at pH 4.00–12.00 (Tong and Li 1986; Lan et al. 2007; Lalvani et al. 1998; Mohan and Pittman 2006).

As shown by Eq. (4), the negatively charge adsorbate molecule was attached to the $–NH_3^+$ group of CSB after releasing the acetate ion. The protonated silanol groups in CSB also support the attachment of adsorbate molecules, as shown by Eq. (5). The different charges between the adsorbate and adsorbent provide an electrostatic attraction between both molecules, thus generating a favorable effect on the adsorption rate. The mechanism proposed in Eq. (4) was performed by Cr(VI) through the formation of a coordination complex with a free electron pair from the group $–NH_3^+$ group of CSB. Meanwhile, MO as an organic compound is only able to interact with the adsorbate through weak van der Waals forces with the $–OH_2^+$ group of CSB as shown in Eq. (5). The addition of long-chain saponin helps to stabilize the adsorbent so that the ability of the adsorbent to attract the adsorbate molecule becomes stronger.

$$CSB–NH_3^+CH_3COO^- + X^- \rightleftharpoons CSB–NH_3^+ \text{---} X^- + CH3COO^- \quad (4)$$

$$CSB–OH_2^+ + X^- \text{or } Y^- \rightleftharpoons CSB–OH_2^+ \text{---} X^- \text{or } Y^- \quad (5)$$

where X = $HCrO_4$ and Y = MO-SO_3.

In contrast, when the pH of the solution exceeds pH_{pzc}, the the surface charges of the adsorbate and adsorbent are both negative. The increasing of pH causes adsorbent protonation to weaken and deprotonation to occur, specifically $–NH_3^+$ to $–NH_2$ (from chitosan) and $–OH_2^+$ to –OH (from bentonite). Since adsorbent and adsorbate both have negative charge, they tend to repulse each other, thus causing decrease in removal efficiency.

The highest removal efficiency did not occur at very acidic pH (2.00–3.00) because at those pH levels, both adsorbate and adsorbent have positive charge. At very acidic pH, Cr(VI) has a high positive redox potential in the range of 1.33 and 1.38 V (Kotaś and Stasicka 2000) that cause high oxidation tendency. The oxidation is triggered by the presence of a considerable number of H^+; thus, the reaction proceeds as shown in Eq. (6).

$$HCrO_4^- + 7H^+ + 3e^- \rightleftharpoons Cr^{3+} + 4H_2O \quad (6)$$

At acidic pH, Cr^{3+} forms complex compounds such as $Cr(OH)^{2+}$ and $Cr(OH)_2^+$ (Angkawijaya et al. 2011; Vinokurov et al. 2004). The presence of positively charged adsorbate cause reduction in the electrostatic attraction, thus

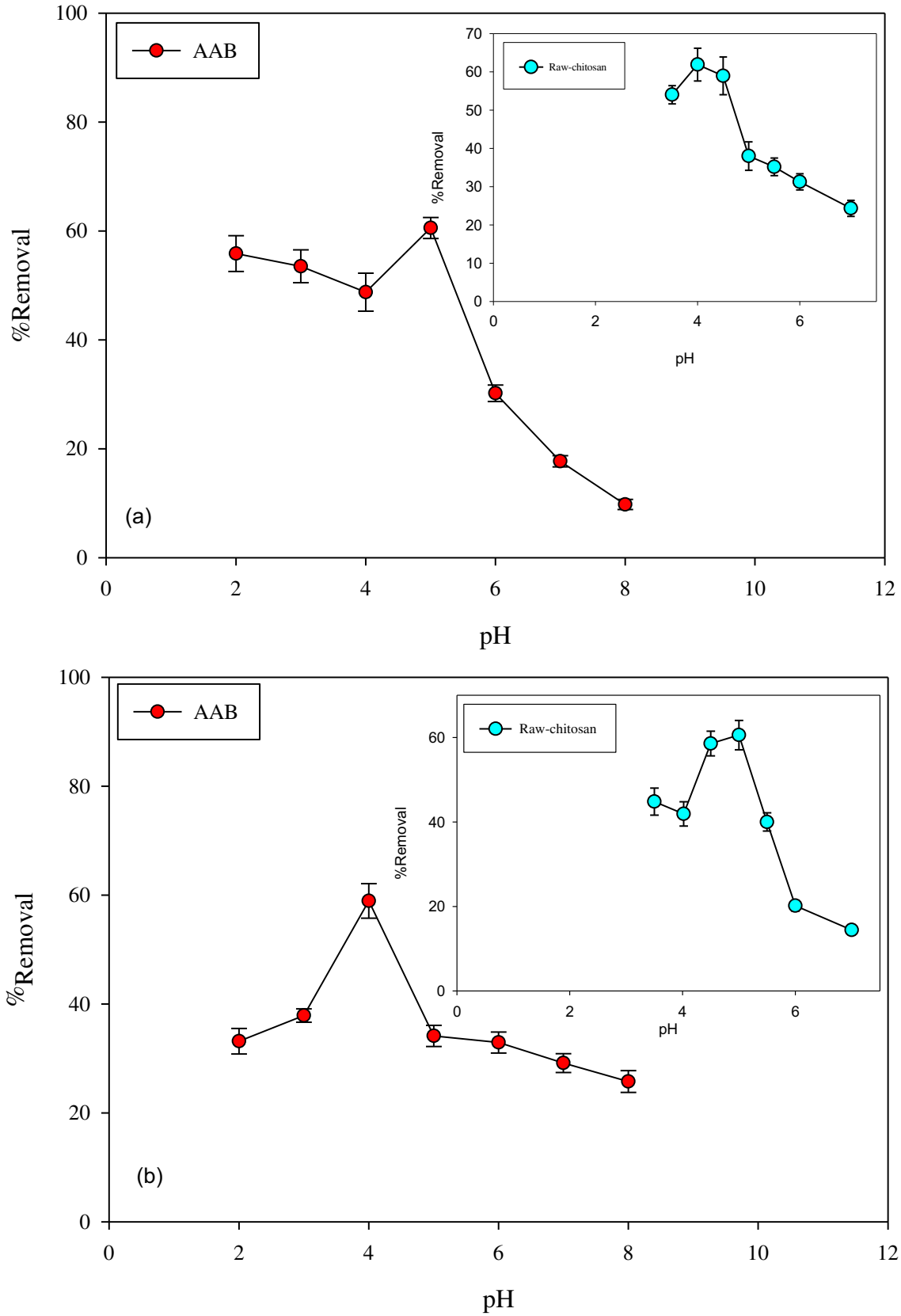

Fig. 3 The effect of pH on the adsorption of **a** MO and **b** Cr(VI). Contact time = 3 h, C_0 = 500 ppm, T = 30 °C, mass of the adsorbent = 0.5 g, V = 0.1 l

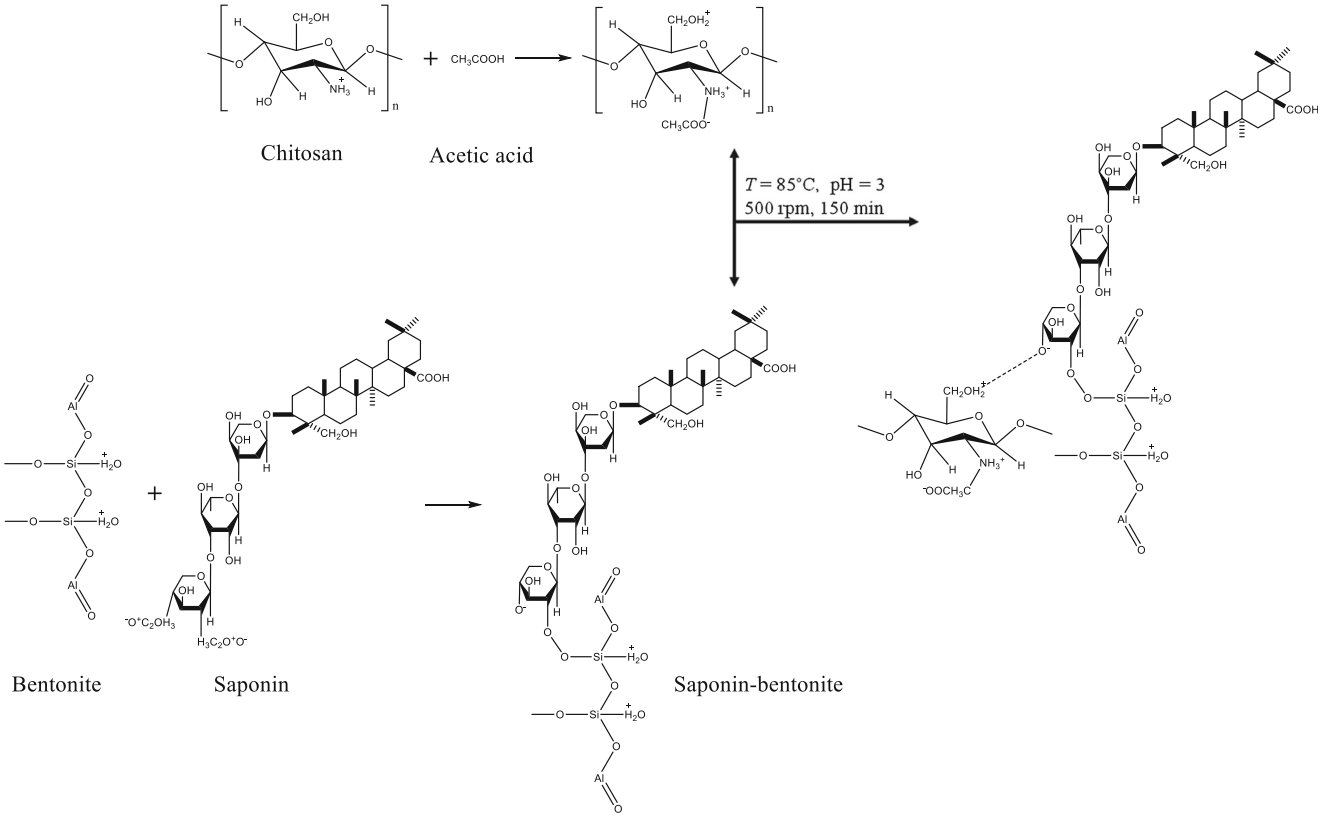

Fig. 4 Schematic illustration indicating the possible interaction between materials during CSB film preparation

lowering the removal efficiency. While for MO, at very acidic pH, the excess H^+ attack the dimethylamino group ($-N(CH_3)_2$); thus, the groups become positively charge as $-N^+(CH_3)_2$.

Adsorption isotherm studies

The adsorption isotherm represents the equilibrium distribution between adsorbate molecules with the surface of solid adsorbent at a certain temperature. The adsorption isotherm can be modeled by using mathematical equations called as adsorption equations. Originally, the available adsorption equations were developed to represent the gas phase equilibria. With a small modification, these adsorption equations could be used to represent the liquid phase adsorption equilibria.

In this study, five adsorption isotherm equations are employed to correlate the adsorption of MO and Cr(VI), specifically Langmuir, Freundlich, Redlich-Paterson, Sips, and Toth equations. The Langmuir equation has the form as follows:

$$q_e = q_m \left(\frac{K_L C_e}{1 + K_L C_e} \right) \tag{7}$$

The specificity of the Langmuir model is found in the parameter q_m that indicates the maximum monolayer adsorption capacity of adsorbent, and K_L is known as the Langmuir equilibrium constant (l g^{-1}) that relates to the strength of the adsorbent surface to attract the adsorbate. Another essential characteristic of the Langmuir isotherm can be expressed by the separation factor (R_L) shown in Eq. (8) (Langmuir 1918).

$$R_L = \frac{1}{1 + K_L C_e} \tag{8}$$

The value of R_L represents the isotherm shape (unfavorable if $R_L > 1$, favorable if $0 < R_L < 1$, and irreversible if $R_L = 1$).

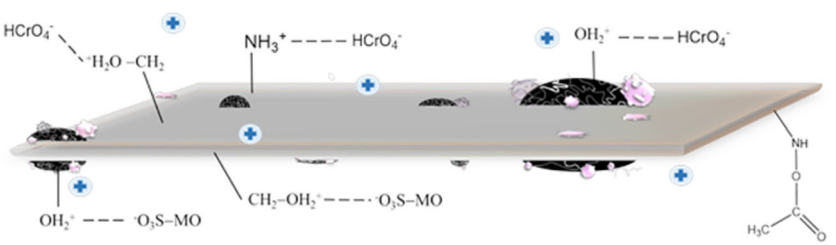

Fig. 5 Electrostatic interactions between cationic groups of CSB film and anionic groups of adsorbate

The Freundlich equation can be expressed as follows:

$$q_e = K_F C_e^{1/n_F} \quad (9)$$

where K_F and n_F correspond to relative adsorption capacity [(mg g^{-1}).(mg l^{-1})$^{1/n}$] and heterogeneity of the adsorption system, respectively. The high value of n_F signifies more heterogeneous adsorbent surface. The parameter n_F is also known as adsorption intensity (Freundlich 1906).

The Redlich-Peterson equation can be expressed as follows:

$$q_e = \left(\frac{K_1 C_e}{1 + K_2 C_e^{\alpha}}\right) \quad (10)$$

Unlike the two previous isotherm models, Redlich and Peterson (1959) have proposed an adsorption model consisting of three parameters to improve the drawback of Langmuir and Freundlich isotherms. Parameters K_1 (l g^{-1}), K_2 (l mg^{-1}), and α are Redlich-Peterson constants that describe the adsorption phenomena in the adsorbent-adsorbate system. The role of α is to characterize the type of isotherm; if $\alpha = 1$, the Redlich-Peterson becomes Langmuir isotherm, whereas if $\alpha = 0$, the Freundlich as a representative of high concentration becomes more approachable. This statement shows the adsorption equilibrium dependent on a wide range of concentrations, presented by the concentration relationships in the numerator and the exponential function in the denominator (Ng et al. 2002). The application of the Redlich-Peterson model can be tested both in a homogeneous or heterogeneous system due to its flexibility.

The Sips equation can be expressed as follows:

$$q_e = q_m \left(\frac{(K_s C_e)^{1/n_s}}{1 + (K_s C_e)^{1/n_s}}\right) \quad (11)$$

Sips proposed a similar equation with the Freundlich equation, but it has a saturation limit capacity for high concentration. Sips model is an empirical isotherm equation based on the distribution of adsorption energy from the surface site of the solid (Sips 1948). The Sips equation consists of parameter K_s that is associated with the affinity constant (l mg^{-1}) and q_m that represents the adsorption capacity (mg g^{-1}).

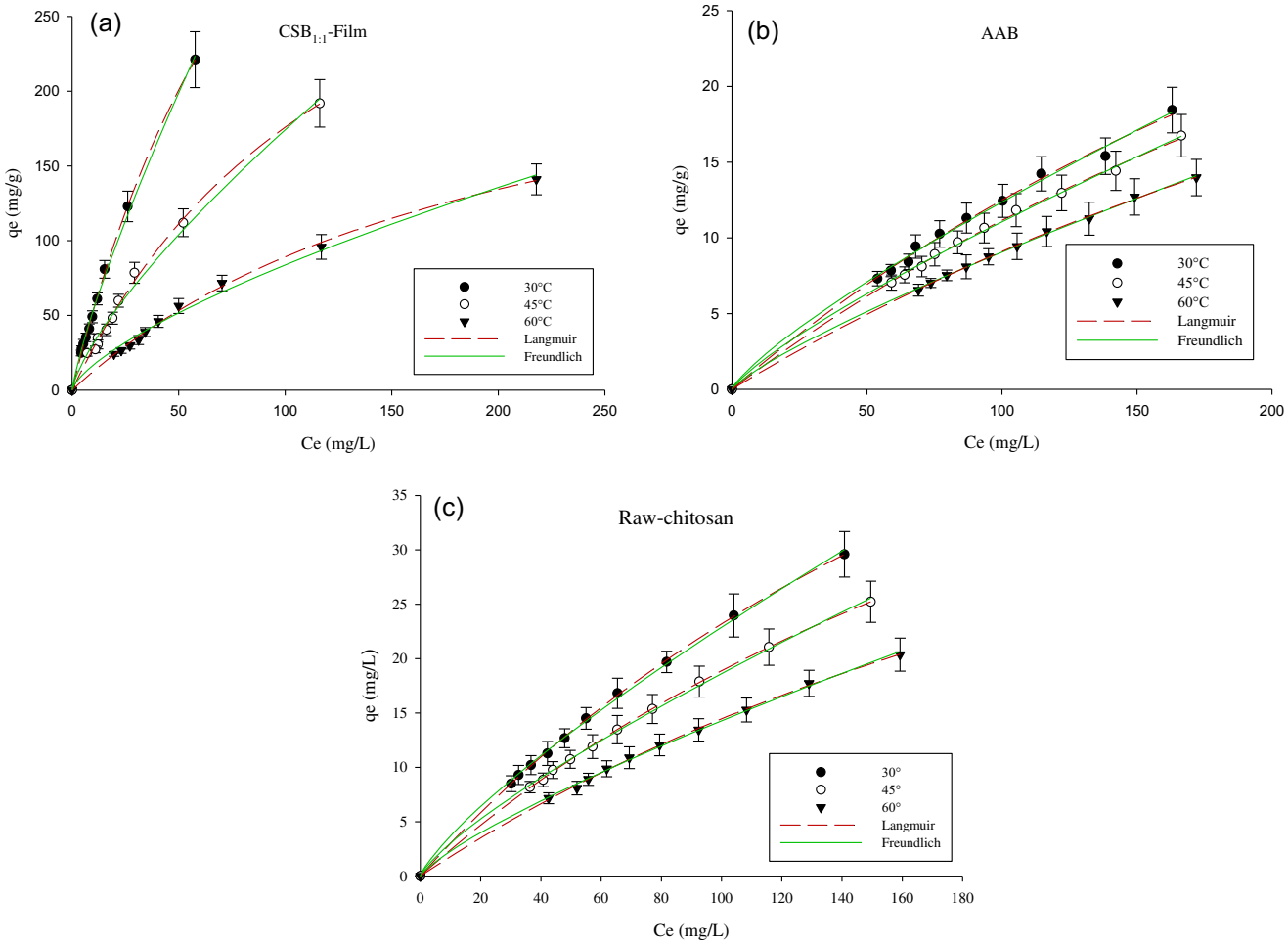

Fig. 6 Adsorption isotherms of Cr(VI) onto **a** $CSB_{1:1}$, **b** AAB, and **c** chitosan

The Toth equation can be expressed as follows:

$$q_e = \frac{q_{tm} K_t C_e}{\left(1 + (K_t C_e)^{n_t}\right)^{1/n_t}} \quad (12)$$

Toth isotherm is a three-parameter adsorption equation since it contains three parameters; Toth equation is usually used to reduce the error between experimental data and the predicted value of equilibrium data. This equation is an empirical model, and it is a modification of the Langmuir equation. The parameter q_{tm} (mg g^{-1}) is the maximum adsorption capacity, K_t describes the adsorption affinity, and n_t is representing the heterogeneity of the adsorption system (Toth 1971; Yuwei and Jianlong 2011).

Since the $CSB_{1:1}$ and $CSB_{2:3}$ gave excellent removal for Cr(VI) and MO, respectively, the complete adsorption isotherm models are represented for those systems only. The adsorption isotherm equilibria of Cr(VI) and MO onto the adsorbents are depicted in Figs. 6 and 7. The fitted parameters of the adsorption isotherm equations are summarized in Table 3. The fitted parameters for AAB and chitosan are provided in Supplementary Data Tables S1 and S2. The results indicate that all the models gave excellent correlation coefficient (R^2). However, to decide the validity of the model, the judgment based on only the correlation coefficient (R^2) is not adequate. Each parameter in each equation should possess correct physical meaning with a reasonable value. The adsorption of MO onto $CSB_{2:3}$, chitosan, and AAB was an endothermic process; it means that the uptake of MO by the adsorbents increased with the increase of temperature. While the adsorption of Cr(VI) onto $CSB_{1:1}$, chitosan, and AAB was an exothermic process, as the temperature increased, the uptake of the Cr(VI) decreased. Parameters q_m and K_f are reasonable and consistent with its physical meaning. However, for other equations, the inconsistency of the parameter values was observed for the adsorption of MO by $CSB_{2:3}$. For the adsorption of Cr(VI), all of the equations can represent the experimental adsorption data very well ($R^2 > 99\%$). All of the parameter values are reasonable and consistent with its physical meanings.

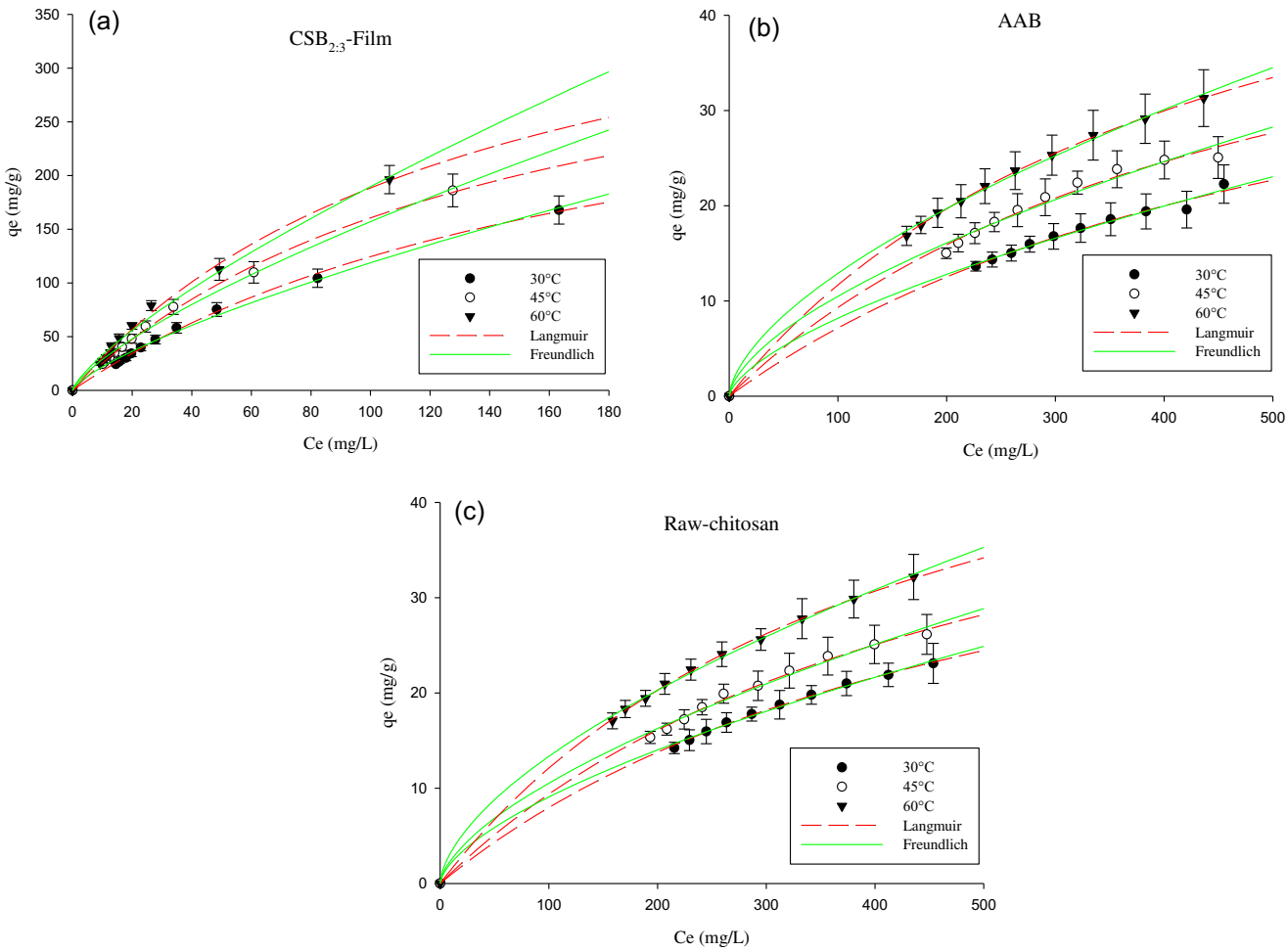

Fig. 7 Adsorption isotherms of MO onto **a** $CSB_{2:3}$, **b** AAB, and **c** chitosan

Table 3 The fitted parameters of several adsorption equations for the adsorption of Cr(VI) onto $CSB_{1:1}$ and MO onto $CSB_{2:3}$

Model	Parameter	$CSB_{1:1}$-Cr(VI)			$CSB_{2:3}$-MO		
		30 °C	45 °C	60 °C	30 °C	45 °C	30 °C
Langmuir	q_m (mg g^{-1})	641.99	56.786	62.843	360.86	398.98	641.99
	K_L (l mg^{-1})	0.0091	0.0020	0.0024	0.0053	0.0067	0.0091
	R_L	0.1802	0.5000	0.4545	0.2740	0.2299	0.1802
	R^2	0.9992	0.9976	0.9996	0.9983	0.9976	0.9992
Freundlich	K_f (mg g^{-1})(mg $l^{-1})^{1/n}$)	8.2748	0.5904	0.8265	4.0094	5.2352	8.2748
	n_f	1.2301	1.5977	1.6554	1.3594	1.3539	1.2301
	R^2	0.9974	0.9955	0.9990	0.9954	0.9955	0.9974
Redlich-Peterson	K_1 (l g^{-1})	5.8595	0.1146	0.1603	2.0634	3.0423	5.8595
	K_2 (l mg^{-1})	0.0095	0.0025	0.0046	0.0159	0.0286	0.0095
	α	0.9907	0.9698	0.9104	0.8158	0.7512	0.9907
	R^2	0.9992	0.9975	0.9996	0.9986	0.9981	0.9992
Sips	q_{sm} (mg g^{-1})	615.98	58.656	63.511	130.14	106.29	615.98
	K_s (l mg^{-1})	0.0095	0.0019	0.0024	0.0159	0.0286	0.0095
	n_s	1.0094	0.9949	0.9984	1.2259	1.3111	1.0094
	R^2	0.9992	0.9976	0.9996	0.9986	0.9981	0.9992
Toth	q_{tm} (mg g^{-1})	658.89	58.065	72.823	527.65	723.83	658.89
	K_t	0.0089	0.0019	0.0022	0.0039	0.0043	0.0089
	n_t	0.9831	0.9850	0.8607	0.7619	0.6738	0.9831
	R^2	0.9992	0.9976	0.9996	0.9985	0.9981	0.9992

As summarized in Table 3, the $CSB_{1:1}$ shows a very high adsorption capacity toward Cr(VI) with q_{max} = 641.99 mg g^{-1}, and $CSB_{2:3}$ shows a similarly high adsorption capacity toward MO with q_{max} = 360.90 mg g^{-1}. It can be seen in Table 4 that the adsorption capacity of CSB are much higher compared to those of other reported adsorbents used for removal of MO and Cr(VI), such as chitosan/organic rectorite composite (5.56 mg MO g^{-1}),

Table 4 The adsorption capacity of various adsorbents involving chitosan, chitosan modification with other materials, and bentonite for MO and Cr(VI)

Adsorbate	Adsorbent	Conditions	q_m (mg g^{-1})	Model	Ref.
MO	Chitosan/organic rectorite composite	C_0 = 10–160 mg/ml, T = 25 °C, t = 80 min	5.56	Langmuir	Zeng et al. 2015
	Bentonite	C_0 = 10–50 ppm, T = 25 °C	33.8	Freundlich	Leodopoulos et al. 2012
	γ-Fe_2O_3/MWCNT/chitosan	T = 25 °C	66.1	Langmuir	Zhu et al. 2010
	Protonated cross-linked chitosan	T = 40 °C	180.2	Langmuir	Huang et al. 2017
	AAB	C_0 = 500 ppm, pH = 4.00–5.00, T = 30 °C, t = 3 h	49.7	Langmuir	This work
	Chitosan		50.8		
	$CSB_{2:3}$		360.9		
Cr (VI)	Chitosan	C_0 = 250–50,000 μg/l, pH = 4.00	35.6	Langmuir	Jung et al. 2013
	Chitosan	C_0 = 500 ppm, pH = 4.00, T = 28 °C, t = 12 h	40	Langmuir	Udaybhaskar et al. 1990
	Chitosan	C_0 = 10–500 mg/l, pH = 4.5	60.24	Langmuir	Li et al. 2015
	Cross-linked chitosan	pH = 3, T = 50 °C, t = 2 h	112.57	Langmuir	Wu et al. 2012
	Electrospun chitosan nanofibers	C_0 = 10–500 mg/l, pH = 4.5	131.58	Freundlich	Li et al. 2015
	Chitosan coated with poly(3-methylthiophene)	C_0 = 200 ppm, pH = 2, T = 70 °C	145.08	Langmuir	Hena 2010
	AAB	C_0 = 200 ppm, pH = 4.07, T = 30 °C, t = 3 h	63.973	Langmuir	This work
	Raw chitosan	C_0 = 200 ppm, pH = 4.02, T = 30 °C, t = 3 h	78.432		
	$CSB_{1:1}$	C_0 = 500 ppm, pH = 4.00–5.00, T = 30 °C, t = 3 h	641.99		

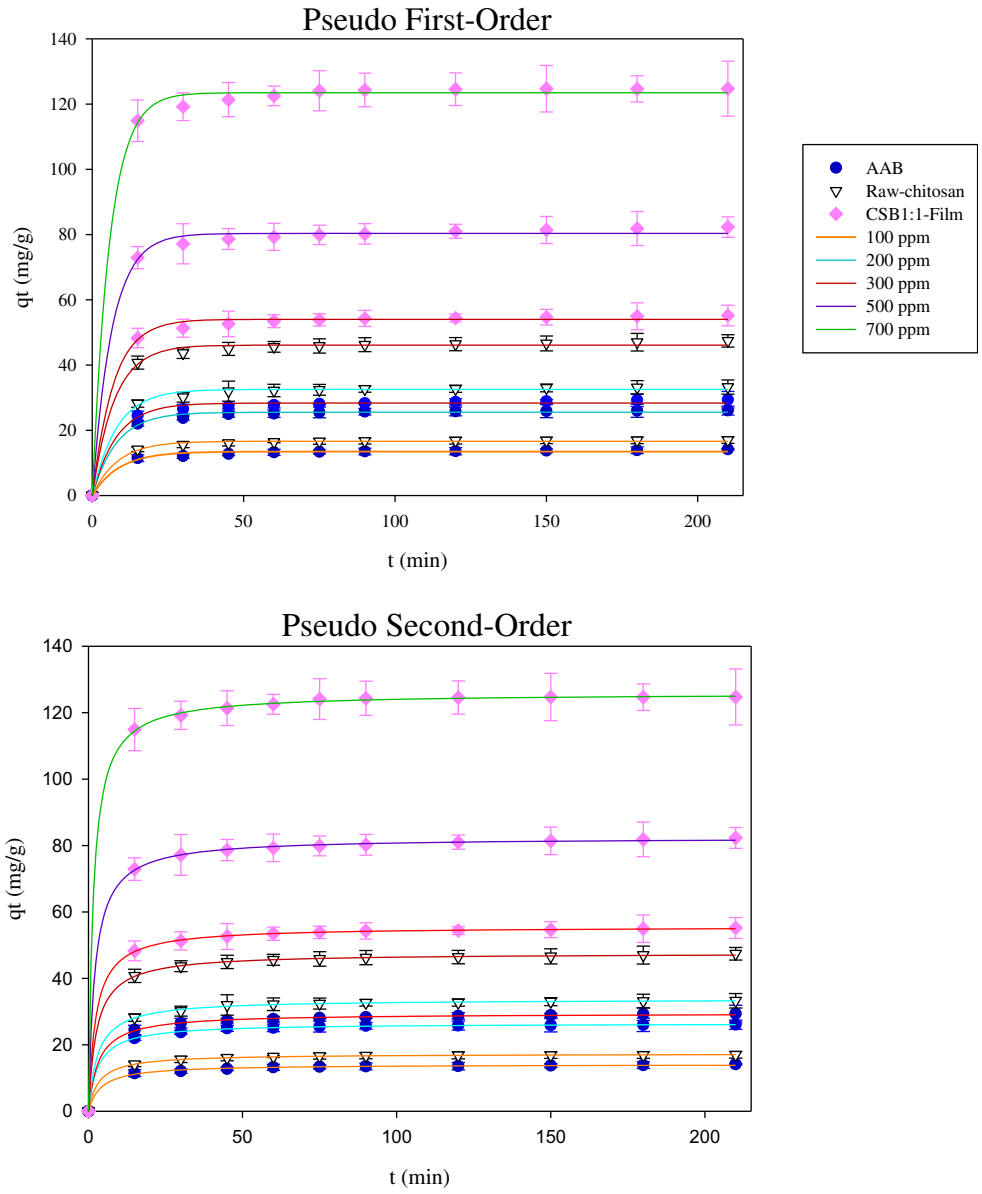

Fig. 8 Pseudo-first- and second-order kinetic sorption of Cr(VI) onto AAB, raw chitosan, and $CSB_{1:1}$

ɣ-Fe_2O_3/MWCNT/chitosan (66.1 mg MO g^{-1}), cross-linked chitosan (112.57 mg Cr g^{-1}), and chitosan coated with poly-3-methyl thiophene (145.08 mg Cr g^{-1}). The reported study also showed that the optimal pH for Cr(VI) removal was at pH 4 which is in accordance with this study. The very high adsorption capacity of CSB shows that CSB is a very promising alternative adsorbent for dye and heavy metal removal.

Kinetic studies

The adsorption kinetics describes the time required for an adsorbent to remove the adsorbate from the solution. The classical models used to correlate the adsorption kinetic data are the pseudo-first- and second-order kinetics models (Plazinski et al. 2009). The pseudo-first-order model or Lagergren equation is presented as:

$$\frac{dq_t}{dt} = k_{1ad}(q_{e1} - q_t) \tag{13}$$

where q_t is the amount of adsorbate per mass of adsorbent at time t (mg g^{-1}), k_{1ad} is the rate constant of pseudo-first-order reaction (min^{-1}), and t is time (min). The integration of Eq. (13) with the boundary conditions: $q_t = 0$ at $t = 0$ and $q_{e1} = q_{e1}$ at $t = t$, produces:

$$q_t = q_{e1}(1 - \exp(-k_{1ad}t)) \tag{14}$$

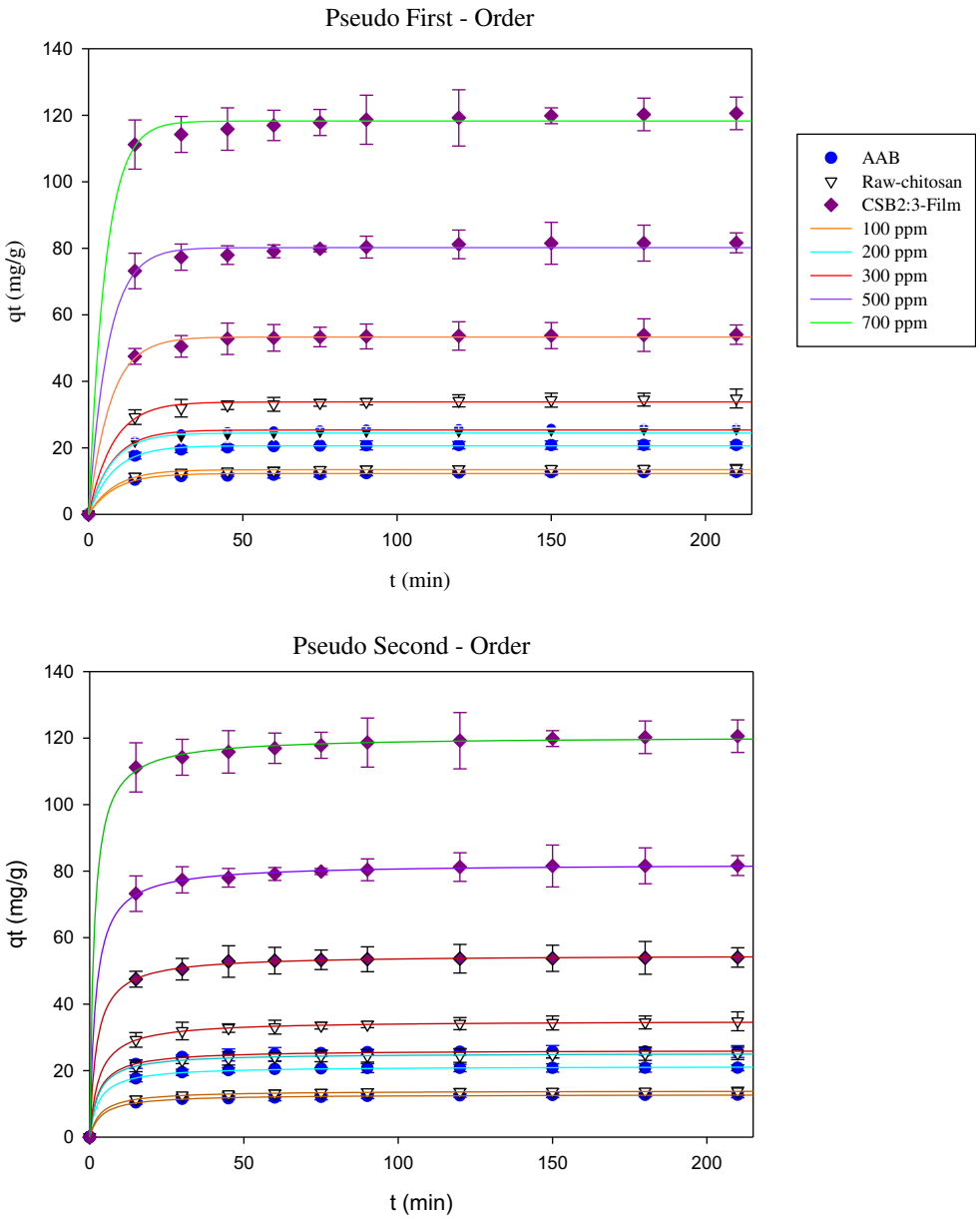

Fig. 9 Pseudo-first- and second-order kinetic sorption of MO onto AAB, raw chitosan, and $CSB_{2:3}$

The pseudo-second-order kinetic can be expressed by the following equation:

$$\frac{d_{qt}}{d_t} = k_{2ad}(q_{e2} - q_t)^2 \tag{15}$$

Integrating Eq. (15) with the same boundary condition as Eq. (13) gives:

$$q_t = q_{e2}\left(\frac{q_{e2}k_{2ad}t}{1 + q_{e2}k_{2ad}}\right) \tag{16}$$

where k_{2ad} is the pseudo-second-order equilibrium rate constant (g mg^{-1} min^{-1}).

The plots of pseudo-first-order and pseudo-second-order for Cr(VI) and MO are given in Figs. 8 and 9, respectively. The fitted parameters are summarized in Table 5; it is evident that the pseudo-second-order could represent the kinetic data better than the pseudo-first-order. In most cases, the pseudo-second-order could serve the adsorption kinetic data better than the pseudo-first-order due to its small sensitivity to the random error of the experiment. The difference between the fitted parameter (q_{e1}) and the experimental data ($q_{e_{exp}}$) are in the range of 0.2412–2.3228 for the pseudo-first-order and 0.0975–0.7524 for the pseudo-second-order. Based on these results, the pseudo-second-order model is more suitable to represent the adsorption kinetics. The initial concentration

Table 5 Pseudo-first- and second-order kinetic parameters for MO and Cr(VI) at various initial concentrations ($T = 30$ °C; $t = 210$ min; and mass adsorbent = 0.5 g)

Adsorbate initial concentration (ppm)	Exp. result	Pseudo-first-order			Pseudo-second-order		
	$q_{e_{exp}}$ (mg g^{-1})	k_{1ad} (min^{-1})	q_{e1} (mg g^{-1})	R_1^2	k_{2ad} (mg g^{-1} min^{-1})	q_{e2} (mg g^{-1})	R_2^2
MO	$CSB_{1:1}$						
300	55.1710	0.1439	53.9881	0.9965	0.0077	55.5502	0.9999
500	82.3233	0.1542	80.3680	0.9970	0.0060	82.4164	0.9998
700	124.7331	0.1734	123.5182	0.9982	0.0053	125.8870	0.9999
Cr(VI)	$CSB_{2:3}$						
300	54.0207	0.1419	53.3141	0.9979	0.0080	54.7731	0.9997
500	81.6566	0.1583	80.2086	0.9970	0.0064	82.1708	0.9997
700	120.6154	0.1833	118.2926	0.9974	0.0059	120.5179	0.9996

of the solute gave a significant effect on the time required to reach the equilibrium condition as indicated by the decrease of k_{2ad} as the initial concentration increase.

Thermodynamic analysis

The information about the thermodynamics of adsorption is very crucial to provide a better understanding of the adsorption process. The thermodynamic of adsorption includes Gibb's free energy change ($\Delta G°$), standard enthalpy change ($\Delta H°$), and standard entropy change ($\Delta S°$).

Equation (17) can be used to determine $\Delta G°$ which shows the spontaneity of the adsorption system.

$$\Delta G^{\circ} = -RT\ln K \tag{17}$$

where R represents the ideal gas constant and K is the thermodynamic equilibrium constant which represents the linear sorption distribution coefficient. In an adsorption process, K is the ratio between the activity of the adsorbed adsorbate (a_s) and the activity of adsorbate at equilibrium (a_e). a_s depends on the activity coefficient (γ_s) and the amount of solute adsorbed (q_e), while a_e depends on the activity coefficient (γ_e) and the amount of solute at equilibrium (C_e). As the amount of solute approaches zero, the activity coefficient is close to 1; thus, K can be obtained by plotting $\ln(q_e/C_e)$ vs. q_e and extrapolating q_e to zero. The parameter $\Delta G°$ has a unit of kJ mol^{-1}, R has a unit of kJ mol^{-1} K^{-1}, and T has a unit of K; from dimensional analysis, the unit of K must be dimensionless. Since the adsorption was done in aqueous solution, K has a unit of l mol^{-1}. K can be calculated as a dimensionless parameter by multiplying it with number of moles of water per liter of solution (55.5 mol l^{-1}) (Milonic 2007; Cadaval et al. 2015).

The relationship between $\Delta G°$, $\Delta H°$, and $\Delta S°$ is shown by Eq. (18):

$$\Delta G^{\circ} = \Delta H^{\circ} - T.\Delta S^{\circ} \tag{18}$$

For the determination of $\Delta H°$ and $\Delta S°$, the above equation can be written as:

$$\ln(55.5\ \mathrm{K}) = \frac{\Delta S^{\circ}}{R} - \frac{\Delta H^{\circ}}{RT} \tag{19}$$

Equation (19) is the classical Van't Hoff equation, and the values $\Delta H°$ and $\Delta S°$ can be determined from the slope and intercept of the Van't Hoff plot between ln K and $1/T$ (Fig. 10). The thermodynamic properties of Cr(VI) and MO adsorption are presented in Table 6.

The adsorption of Cr(VI) and MO in all systems give a negative $\Delta G°$ suggesting that the adsorption processes are favorable and spontaneous; thus, the desorption process can not occur naturally. In adsorption of Cr(VI), the $\Delta G°$ is increasing as the T increased, indicating that the adsorption process is more favorable at low temperature. In adsorption of MO, the $\Delta G°$ is decreasing as the T increased, thus confirming that the adsorption of MO is more suitable at high temperatures.

The $\Delta S°$ shows randomness of the adsorption system. Positive $\Delta S°$ value indicates an increase in the randomness of the adsorption system due to the high affinity of the adsorbate molecule for the active adsorbent site. Negative $\Delta S°$ indicates low randomness (reaching stationary conditions) on the surface of the solid adsorbent. The $\Delta S°$ for the adsorption of MO in all systems is positive as indicated in Table 6; it means that the adsorption process is disordered due to the complexity of the adsorption system, while for the adsorption of Cr(VI), the adsorption system is more ordered. In the adsorption system of MO by adsorbents, the positive value of $\Delta H°$ is found, indicating that the adsorption of MO is endothermic, while $\Delta H°$ is negative for Cr(VI) adsorption, indicating that the process is exothermic.

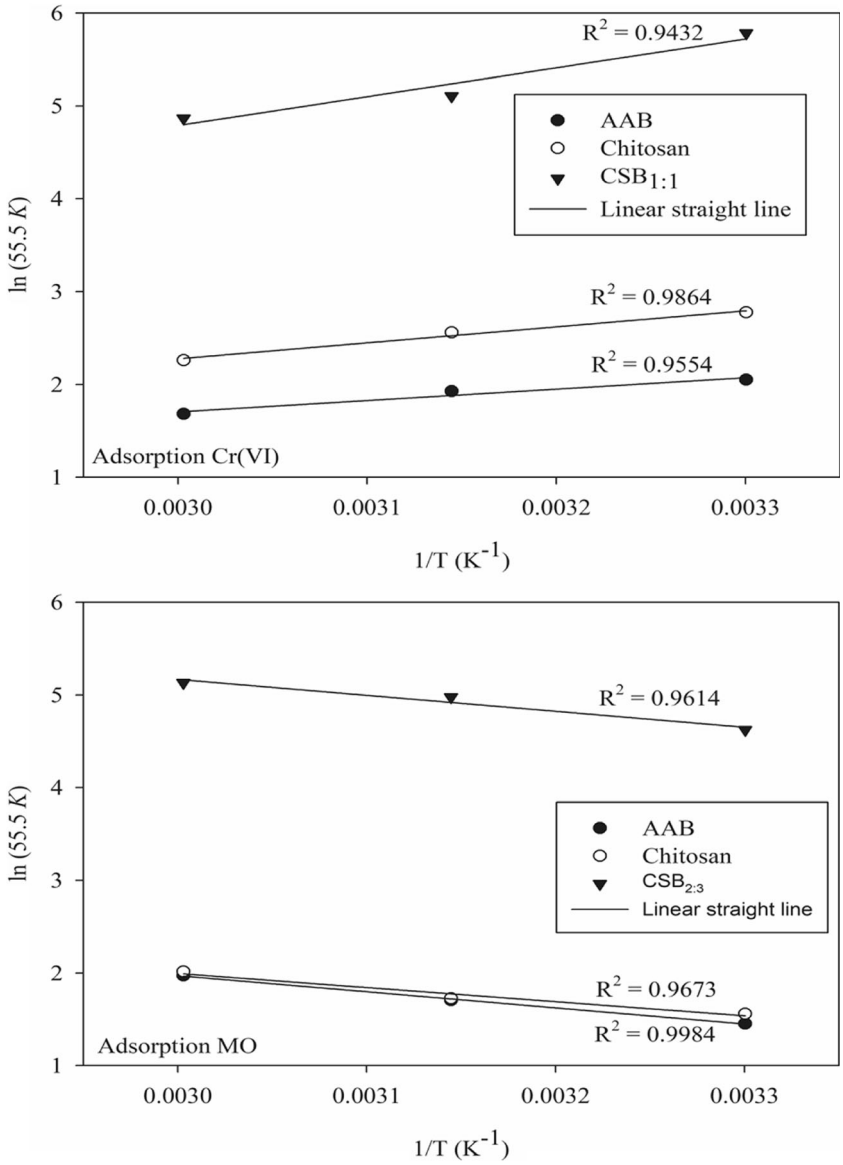

Fig. 10 Determination of the adsorption thermodynamic properties

Conclusion

Chitosan-saponin-bentonite composite films (CSB) have been successfully prepared in this study. The CSB show a high removal efficiency and high adsorption capacity toward MO and Cr(VI) in the aqueous phase. These CSB have significantly higher adsorption capacity in acidic conditions pH 4.00–5.00, and the equilibrium condition was achieved within 3 h.

Table 6 The adsorption thermodynamic properties

Adsorbate	Type of adsorbent	$\Delta G°$ (kJ mol^{-1})			$\Delta H°$ (kJ mol^{-1})	$\Delta S°$ (J mol^{-1} K^{-1})
		303 K	318 K	333 K		
Cr(VI)	AAB	− 5.1658	− 5.0935	− 4.6590	− 10.2251	− 16.5168
	Chitosan	− 6.9903	− 6.7616	− 6.2568	− 14.3536	− 24.1636
	$CSB_{1:1}$	− 14.5679	− 13.5024	− 13.4737	− 25.7924	− 37.5616
MO	AAB	− 3.6601	− 4.5126	− 5.4589	14.4914	59.8594
	Chitosan	− 3.9269	− 4.5616	− 5.5788	12.6929	54.6604
	$CSB_{2:3}$	− 11.6443	− 13.1626	− 14.2099	14.3457	86.0110

Five well-known adsorption isotherm equations (Langmuir, Freundlich, Redlich-Peterson, Sips, and Toth) were employed to correlate the adsorption data. Most of the models could correlate data well (except for $CSB_{2:3}$-MO system, Sips and Toth failed to give consistent and reasonable parameter values). The kinetic behavior as a function of time and concentration for two types of adsorbates can be explained well by the pseudo-second-order model. The thermodynamic study of adsorption illustrates that the adsorption of MO is spontaneous and endothermic, while the adsorption of Cr(VI) is spontaneous and exothermic.

Funding information Financial support from the Ministry of Research and Technology and Higher Education through Fundamental Research grant is highly appreciated.

References

Angkawijaya AE, Fazary AE, Hernowo E, Taha M, Ju YH (2011) Iron(III), chromium(III), and copper(II) complexes of $_L$-norvaline and ferulic acid. J Chem Eng Data 56:532–540

Bahranowski K, Gawel A, Klimek A, Michalik-Zym A, Napruszewska BD, Nattich-Rak M, Rogowska M, Serwicka EM (2017) Influence of purification method of Na-montmorillonite on textural properties of clay mineral composites with TiO2 nanoparticles. Appl Clay Sci 140:75–80

Bassyouni DG, Hamad HA, El-Ashtoukhy E-SZ, Amin NK, El-Latif MMA (2017) Comparative performance of anodic oxidation and electrocoagulation as clean processes for electrocatalytic degradation of diazo dye acid Brown 14 in aqueous medium. J Hazard Mater 335:178–187

Bhattacharyya R, Ray SK (2015) Removal of Congo red and methyl violet from water using nano clay filled composite hydrogels of poly acrylic acid and polyethylene glycol. Chem Eng J 260:269–283

Cadaval TRS, Dotto GL, Pinto LAA (2015) Equilibrium isotherms, thermodynamics and kinetic studies for the adsorption of food azo dyes onto chitosan films. Chem Eng Commun 202:1316–1323

Chiou MS, Li HY (2002) Equilibrium and kinetic modeling of adsorption of reactive dye on cross-linked chitosan beads. J Hazard Mater 93: 233–248

Crini G, Badot PM (2008) Application of chitosan, a natural amino polysaccharide, for dye removal from aqueous solutions by adsorption processes using batch studies: a review of recent literature. Prog Polym Sci 33:399–447

Dotto GL, Moura JM, Cadaval TRS, Pinto LAA (2013) Application of chitosan films for the removal of food dyes from aqueous solutions by adsorption. Chem Eng J 214:8–16

Freundlich HMF (1906) Over the adsorption in solution. J Phys Chem 57: 385–471

Hamdaoui O (2006) Batch study of liquid-phase adsorption of methylene blue using cedar sawdust and crushed brick. J Hazard Mater 135: 264–273

Hena S (2010) Removal of chromium hexavalent ion from aqueous solutions using biopolymer chitosan coated with poly 3-methyl thiophene polymer. J Hazard Mater 181:474–479

Hou H, Zhou R, Wu P, Wu L (2012) Removal of Congo red dye from aqueous solution with hydroxyapatite/chitosan composite. Chem Eng J 211-212:336–342

Hu XJ, Wang JS, Liu YG, Li X, Zeng GM, Bao ZL, Zeng XX, Chen AW, Long F (2011) Adsorption of chromium (VI) by ethylenediamine-modified cross-linked magnetic chitosan resin: isotherms, kinetics, and thermodynamics. J Hazard Mater 185:306–314

Huang R, Liu Q, Huo J, Yang B (2017) Adsorption of methyl orange onto protonated cross-linked chitosan. Arab J Chem 10:24–32

Jung C, Heo J, Han J, Her N, Lee SJ, Oh J, Ryu J, Yoon Y (2013) Hexavalent chromium removal by various adsorbents: powdered activated carbon, chitosan, and single/multi-walled carbon nanotubes. Sep Purif Technol 106:63–71

Kotaś J, Stasicka Z (2000) Chromium occurrence in the environment and methods of its speciation. Environ Pollut 107:263–283

Kurniawan A, Sutiono H, Ju YH, Soetaredjo FE, Ayucitra A, Yudha A, Ismadji S (2011) Utilization of rarasaponin natural surfactant for organo-bentonite preparation: application for methylene blue removal from aqueous effluent. Microporous Mesoporous Mater 142:184–193

Lalvani SB, Wiltowski T, Hübner A, Weston A, Mandich N (1998) Removal of hexavalent chromium and metal cations by a selective and novel carbon adsorbent. Carbon 36:1219–1226

Lan Y, Deng B, Kim C, Thornton EC (2007) Influence of soil minerals on chromium (VI) reduction by sulfide under anoxic conditions. Geochem Trans 8:4

Langmuir I (1918) The adsorption of gases on plane surfaces of glass, mica and platinum. J Am Chem Soc 40:1361–1403

Laysandra L, Sari MWMK, Soetaredjo FE, Foe K, Putro JN, Kurniawan A, Ju YH, Ismadji S (2017) Adsorption and photocatalytic performance of bentonite-titanium dioxide composites for methylene blue and rhodamine B decoloration. Heliyon 3:e00488

Leodopoulos C, Doulia D, Gimouhopoulos K, Triantis TM (2012) Single and simultaneous adsorption of methyl orange and humic acid onto bentonite. Appl Clay Sci 70:84–90

Li L, Li Y, Cao L, Yang C (2015) Enhanced chromium (VI) adsorption using nanosized chitosan fibers tailored by electrospinning. Carbohydr Polym 125:206–213

Milonic SK (2007) A consideration of the correct calculation of thermodynamic parameters of adsorption. J Serb Chem Soc 72:1363–1367

Mohan D, Pittman CU (2006) Activated carbons and low cost adsorbents for remediation of tri- and hexavalent chromium from water. J Hazard Mater 137:762–811

Ng JCY, Cheung WH, McKay G (2002) Equilibrium studies of the sorption of Cu(II) ions onto chitosan. J Colloid Interface Sci 255:64–74

Oh Y, Armstrong AL, Finnerty C, Zheng S, Hu M, Torrents A, Mi B (2017) Understanding the pH-responsive behavior of graphene oxide membrane in removing ions and organic micropollutants. J Membr Sci 541:235–243

Paluszkiewicz C, Stodolak E, Hasik M, Blazewicz M (2011) FT-IR study of montmorillonite-chitosan nanocomposite materials. Spectrochim Acta A Mol Biomol Spectrosc 79:784–788

Plazinski W, Rudzinski W, Plazinska A (2009) Theoretical models of sorption kinetics including a surface reaction mechanism: a review. Adv Colloid Interf Sci 152:2–13

Redlich O, Peterson DL (1959) A useful adsorption isotherm. J Phys Chem 63:1024–1024

Santoso SP, Laysandra L, Putro JN, Lie J, Soetaredjo FE, Ismadji S, Ayucitra A, Ju YH (2017) Preparation of nanocrystalline cellulose-montmorillonite composite via thermal radiation for liquid-phase adsorption. J Mol Liq 233:29–37

Shanmuganathan S, Loganathan P, Kazner C, Johir MAH, Vigneswaran S (2016) Submerged membrane filtration adsorption hybrid system for the removal of organic micropollutants from a water reclamation plant reverse osmosis concentrate. Desalination 401:134–141

Sips R (1948) On the structure of a catalyst surface. J Chem Phys 16:490–495

Tahir SS, Rauf N (2006) Removal of a cationic dye from aqueous solutions by adsorption onto bentonite clay. Chemosphere 63:1842–1848

Tong SY, Li KA (1986) The distribution of chromium(VI) species in solution as a function of pH and concentration. Talanta 33:775–777

Toth J (1971) State equations of solid-gas interface layers. Acta Chim Acad Sci Hungaricae 69:311–317

Udaybhaskar P, Iyengar L, Rao AVSP (1990) Hexavalent chromium interaction with chitosan. J Appl Polym Sci 39:739–747

Vinokurov EG, Kuznetsoz V, Bondar V (2004) Aqueous solutions of Cr(III) sulfate: modeling of equilibrium composition and physicochemical properties. Russ J Coord Chem 30:496–504

Walker GM, Hansen L, Hanna JA, Allen SJ (2003) Kinetics of a reactive dye adsorption onto dolomitic sorbents. Water Res 37:2081–2089

Wan X, Zhan Y, Long Z, Zeng G, He Y (2017) Core@double-shell structured magnetic halloysite nanotube nano-hybrid as efficient recyclable adsorbent for methylene blue removal. Chem Eng J 330: 491–504

Wu Z, Li S, Wan J, Wang Y (2012) Cr(VI) adsorption on an improved synthesised cross-linked chitosan resin. J Mol Liq 170:25–29

Yuwei C, Jianlong W (2011) Preparation and characterization of magnetic chitosan nanoparticles and its application for Cu(II) removal. Chem Eng J 168:286–292

Zeng L, Xie M, Zhang Q, Kang Y, Guo X, Xiao H, Peng Y, Luo J (2015) Chitosan/organic rectorite composite for the magnetic uptake of methylene blue and methyl orange. Carbohydr Polym 123:89–98

Zhan Y, Wan X, He S, Yang Q, He Y (2017) Design of durable and efficient poly(arene ether nitrile)/bioinspired polydopamine coated graphene oxide nanofibrouscomposite membrane for anionic dye separation. Chem Eng J 330:491–504

Zhan Y, He S, Wan X, Zhang J, Liu B, Wang J, Li Z (2018) Easy-handling bamboo-like polupyrrole nanofibrous mats with high adsorption capacity for hexavalent chromium removal. J Colloid Interface Sci 529:385–395

Zhang L, Hu P, Wang J, Liu Q, Huang R (2015) Adsorption of methyl orange (MO) by Zr(IV)-immobilized cross-linked chitosan/bentonite composite. Int J Biol Macromol 81:818–827

Zhu HY, Jiang R, Xiao L, Zeng GM (2010) Preparation, characterization, adsorption kinetics and thermodynamics of novel magnetic chitosan enwrapping nanosized γ-Fe2O3and multi-walled carbon nanotubes with enhanced adsorption properties for methyl orange. Bioresour Technol 101:5063–5069